Modeling and field-experiments identification of vertical dynamics of vehicle with active anti-roll bar

R. Tavares, M. Ruderman
University of Agder (UiA)
Grimstad, Norway
rafael.tavares@uia.no, michael.ruderman@uia.no

D. Menjoie, J. Vazquez Molina, M. Dhaens
DRiV, Tenneco Automotive BVBA
Sint-Truiden, Belgium
mdhaens@driv.com

***Abstract*—This paper deals with modeling and identification of vertical dynamics of the ground vehicle equipped with two active anti-roll torsion bars. A series of field tests of a full-scale drive have been performed, from which multiple displacement and acceleration data of the unsprung and sprung masses have been collected for each vehicle corner. The standard full vertical vehicle model is extended by the developed model of an active anti-roll torsion bar and valve-controlled semi-active shock absorbing damper. Along with the three-dimensional damping map, the nonlinear progressive stiffness of the elastomer-based decoupling unit are identified from the available data. The multi-channel and multi-state linearized dynamic system model is also obtained. Several MIMO transfer characteristics are exemplary shown for comparing the measured frequency response functions and those estimated from the input-output behavior of the full model. The vehicle setup with the anti-roll bars and performed field tests are described along with the drive trajectories and road excitation conditions.**

***Index Terms*—Vehicle dynamics, Modeling, System identification, Nonlinear curve fitting, State-space model, MIMO**

I. Introduction

Increasing ride comfort while keeping the desirable vehicle handling and, above all, safety require in particular a detailed analysis of the vertical dynamics, including the behavior of embedded active and/or semi-active components of the vehicle suspension system. Even though active damping in road vehicle suspension systems fell since long into the focus of intensive research, see e.g. [1], and reached nowadays a certain maturity, it is also well-known that the spring and damper characteristics required for good handling on a vehicle are not the same as those required for good ride comfort [2]. Thanks to a continuing increase in the efficiency and compatibility of integrated and embedded mechatronic systems in automotive, see e.g. [3], more and more innovative and original technologies emerged as available for design of active and semi-active suspension systems. The development of such innovative components almost always appears hand in hand with the suspension control, at higher-level for the vertical and correspondingly anti-roll dynamics, and at lower-level for the integrated active elements like controlling valves and motors. For an overview of state of the art in active and semi-active suspension control systems we refer e.g. to [4].

One of such mechatronic components used for stabilizing and improving the vertical dynamics is an active anti-roll bar, commercially available and used in the car industry, see e.g. [5]. Apart from passive anti-roll bars, various active counterparts have been proposed along with different actuator and control solutions, like for example one with servo-valve hydraulic actuators [6]. Another, compact solution with a geared-motor has been proposed in [7], where a torsion-bar-based active roll control constitutes a key functionality, see e.g. [8], for drive comfort and safety. Only few works dedicated to a virtual (simulator-based) and laboratory testing can be found on that, like for example [9], while a field-based identification and validation of the associated dynamic models remain in focus of the ongoing research. A dynamics-faithful modeling has to be also compatible with the full vertical vehicle models, while for the single corner (so-called quarter-vehicle model) an elaborated approach has been recently proposed in [10]. It is also worth noting that despite the full vertical vehicle models have been well established and accommodated in the standard automotive literature, see e.g. [11], the inherent limitations of different vehicle models, especially for the roll dynamics, have to be taken into account when incorporating the active anti-roll components [12].

This paper reports the modeling and experimental analysis of vertical dynamics of the vehicle with active anti-roll bar, based on the field experiments of the full-scale drive. The vehicle model is based on the state of the art standard passive vertical dynamic full-vehicle model [11], with defined vehicle geometry and standard quarter-car suspension on each chassis corner. The entire vertical vehicle modeling is extended by capturing the principal dynamics of the active anti-roll torsion bar and the nonlinear semi-active damper. Two dedicated nonlinear mapping functions of the stiffness and adjustable damping components are proposed and accurately fitted on the available system data. The required linearizing step is also made towards the MIMO (multiple-input-multiple-output) system approximation, which then allows for a frequency response analysis of the real measured data compared with the different channels transfer function. The rest of the paper is organized as follows. The principle hardware and instrumentation setup of the vehicle are briefly explained in section II. The full vertical dynamics modeling, including kinematics, active elements, and all nonlinear components are provided in section III. The accomplished field experiments are summarized in section IV, while the performed system identification is described in detail in section V. The paper is

Author´s accepted manuscript
The manuscript accepted to publication in
IEEE International Workshop on Advanced Motion Control (AMC2020)

concluded by section VI.

II. Vehicle setup

The test vehicle used in this study was a sport utility vehicle (SUV) equipped with an Active Roll Control (eARC) [7] as presented in Fig. 1a. The suspension technology in this vehicle comprises a double wishbone on the front axle and a multi-link on the rear axle, each corner equipped with an semi-active air spring damper.

The electro-mechanical actuator (see Fig. 1b), consisting of a brushless (BLDC) motor, three-stage planetary gearbox, two torsion bar segments with elastic decoupling unit, and torque sensor, provides highly dynamic response. The operation on a single axle includes controlling two main functions – the disturbance decoupling and anti-roll support [8], [13].

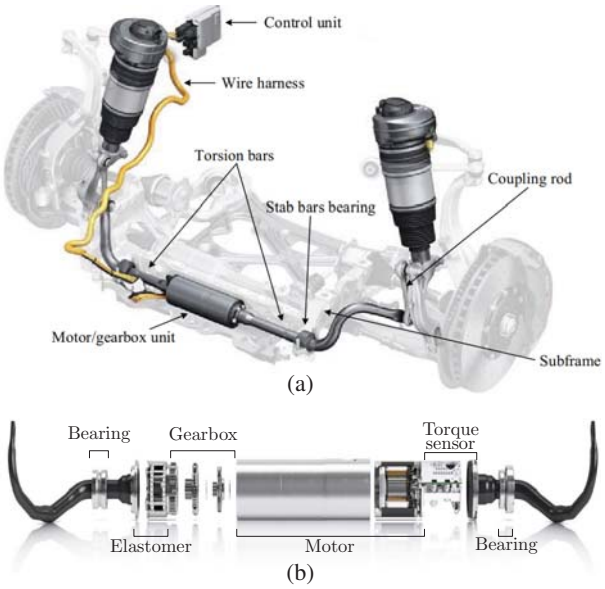

Fig. 1: eARC: (a) integrated in front axle of a SUV [9]; (b) section of actuator assembly ([8]).

The 48 V powered BLDC motor can peak electrical loads at 1.5 kW per axle, corresponding to a maximum actuation torque of 1200 Nm [13]. The torsional load given by the relative rotation between the two stabilizer halves is decoupled from the geared-motor by an elastic decoupling unit [8]. This elastomer, whose rotational rigidity is lower than the rotational rigidity of the stabilizer halves, permits angular displacement between the two halves without appreciable rotation at the intermediately connected slewing motor. Therefore, the system exhibits nonlinear torsional characteristics, mainly due to elastic decoupling unit, between the overall torque M_a of the bar and overall angular displacement θ_a of the actuator. The following chain of components connected in series constitute the actuator assembly: left halve torsion bar, the elastomer decoupling unit, three-stages planetary gearbox, BLDC motor, torque sensor and the right halve torsion bar. The whole actuator assembly is allowed to rotate, guided by two bearings that house each halve torsion shaft into the chassis. Each torsion bar end then is fixed to the corresponding suspension strut. The generated motor torque M_m compensates the vehicle roll (θ) through the binary of equal and symmetric actuator forces F_a transmitted to the two suspension rods on each side of the axle.

The test vehicle was instrumented for further system identification based on the field test measurements. Multiple accelerometers from TE connectivity (models 4604-010 and 4604-050) were placed for measuring the wheels (unsprung masses) and chassis (sprung mass) accelerations as follows: 4 placed in each wheel (Z coordinate), 4 placed on each corner on the bottom side of the rockers of the chassis (XYZ coordinate), and in addition 4 accelerometers were installed in the frame of the driver's seat. Displacement laser sensors (ELAG Optimess MC 400) were placed on each bumper corner for measurement of the absolute displacement between chassis and the road. Two current transducers (LEM AT50B10) measure the currents for each BLDC motor of eARC, i.e. on each axle. Two additional current transducers measure the solenoid currents for semi-active damper valves (both on front and rear). The placement of the sensors is shown in Fig. 2. A GPS module was installed on the rooftop for measurement of vehicle trajectory (latitude and longitude) and vehicle velocity. Two synchronization PROSIG units with a total of 32 analog channels were used for data acquisition, with sampling rates of 2.5 kHz for accelerometers, 20 kHz for currents and 20 Hz for GPS signals.

Fig. 2: Vehicle instrumentation: (a) accelerometer on unsprung mass; (b) displacement sensor on the front bumper; (c) current sensor around power input wires.

III. Modeling

In the following, the full-order vertical vehicle model with integrated anti-roll bar and semi-active suspension is given. Subscript indexes i and j are used to indicate the corresponding axle (or corner) of the vehicle, with $i = \{f, r\}$ for the front and rear, and $j = \{l, r\}$ for the left and right.

A. Anti-roll bar

The dynamics of the electrical circuit of BLDC motor are assumed to be much faster compared with dynamic behavior of mechanical parts. Therefore, the angular motion equation for the motor can be written as

$$J_m \ddot{\theta}_m = M_m - M_{fri} - \frac{M_a}{k_g}, \tag{1}$$

where J_m is the moment of inertia of the motor, θ_m is the angular displacement of the motor shaft, and k_g is the three-stage gearbox ratio. The generated motor torque M_m is proportional to the controlled motor current

$$M_m = K_m i_a, \tag{2}$$

with the motor torque constant K_m. The overall torsional actuator torque M_a is given by the nonlinear characteristics

$$M_a = f(\theta_a), \tag{3}$$

and the viscous actuator damping as

$$M_{fri} = b_m \dot{\theta}_m, \tag{4}$$

where b_m is the linear damping coefficient. For each axle $i = \{f, r\}$, the overall actuator angle θ_a is given as a superposition of the bounded angular motor displacement $\min(\theta_m) < \theta_m < \max(\theta_m)$ and the relative angle between both torsion bar halves as

$$\theta_a = \frac{\theta_m}{k_g} - (\theta_{t_{il}} - \theta_{t_{ir}}), \tag{5}$$

where $\theta_{t_{ij}}$ is the torsion angle for each halve torsion bar relative to their initial angular position. By replacing the variables defined in eqs. (2)-(5) into the angular motion equation defined in eq. (1), the dynamics of eARC can be the written, for each axle i, as

$$\begin{aligned} \ddot{\theta}_{m_i} =& \frac{1}{J_m}\left[K_m i_{a_i} - b_m\right] - \\ & \frac{1}{J_m}\left[\dot{\theta}_{m_i} - f(\theta_{a_i})\left(\frac{1}{k_g}\theta_{m_f} - (\theta_{t_{il}} - \theta_{t_{ir}})\right)\right]. \end{aligned} \tag{6}$$

The binary of equal and symmetric actuator forces $F_{a_{il}} = -F_{a_{ir}}$ transmitted to the two suspension struts on each side of the axle are given by

$$F_{a_{ij}} = \frac{M_a}{l_a}, \tag{7}$$

where l_a is the length of each half of the torsion bar.

B. Full vehicle model

A full vertical vehicle model with eARC extension is derived for the assumed three degrees of freedom: roll θ, pitch ϕ, and heave z_s of the chassis, which constitutes the sprung mass m_s. The corresponding diagram free-cut bodies is shown in Fig. 3. The following modeling assumptions have been made: kinematic effects due to suspension geometry are ignored, i.e. the suspensions only provide vertical forces to the chassis; the vehicle chassis plane is parallel to the road; spring initial deflections are due to equilibrium of m_s gravity components [11]. The chassis dynamics are given by

$$\begin{aligned} m_s \ddot{z}_s =& -F_{s_{fl}} - F_{s_{fr}} - F_{s_{rl}} - F_{s_{rr}}, \\ I_{xx}\ddot{\theta} =& \left(F_{s_{rl}} - F_{s_{rr}} + F_{a_{rl}} - F_{a_{rr}}\right) t_r + \\ & \left(F_{s_{fl}} - F_{s_{fr}} + F_{a_{fl}} - F_{a_{fr}}\right) t_f + M_{d_x}, \\ I_{yy}\ddot{\phi} =& \left(F_{s_{rl}} + F_{s_{rr}} + F_{a_{rl}} + F_{a_{rr}}\right) l_r - \\ & \left(F_{s_{fl}} + F_{s_{fr}} + F_{a_{fl}} + F_{a_{fr}}\right) l_f + M_{d_y}, \end{aligned} \tag{8}$$

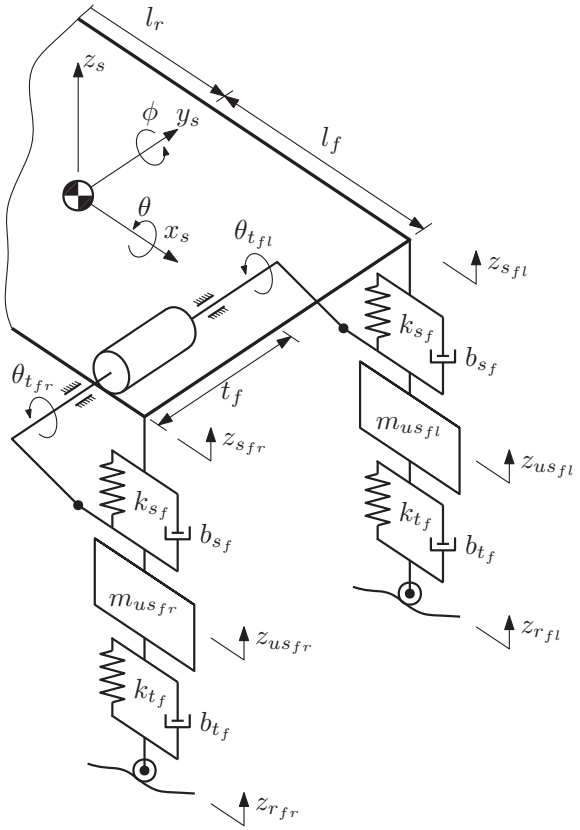

Fig. 3: Front section of the full vehicle model.

where m_s is the sprung mass with inertias I_{xx} and I_{yy}, M_{dx} is the moment about x_s-axis (coming from steering) and M_{dy} is the moment about y_s-axis (coming from accelerating and breaking), cf. Fig. 3. Vehicle geometry is defined by the distances (along x_s-axis) between the center of mass (COM) and the front and rear axles l_f and l_r, and the distances (along y_s-axis) between the COM and the front and rear corners t_f and t_r. The dynamics of each (corner) unsprung mass $m_{us_{ij}}$ are given by

$$m_{us_{ij}} \ddot{z}_{us_{ij}} = F_{s_{ij}} - F_{t_{ij}} + F_{a_{ij}}, \tag{9}$$

where $z_{us_{ij}}$ is the vertical displacement and $z_{r_{ij}}$ is the road input at each corner. The vertical tire and suspension forces, $F_{t_{ij}}$ and $F_{s_{ij}}$ correspondingly, are defined as

$$\begin{aligned} F_{t_{ij}} &= k_{t_i}(z_{us_{ij}} - z_{r_{ij}}) + b_{t_i}(\dot{z}_{us_{ij}} - \dot{z}_{r_{ij}}), \\ F_{s_{ij}} &= k_{s_i}(z_{s_{ij}} - z_{us_{ij}}) + F_d(\dot{z}, i_{d_i}, p_m(i_{d_i})). \end{aligned} \tag{10}$$

Here k_t is tire elastic stiffness, b_t is tire damping coefficient, and k_s is passive spring coefficient. The semi-active damper force, with the control valve current i_{d_i}, is denoted by F_d and further described in section V-C. The kinematic relationships between the COM, with coordinate z_s, and the connection points of each corner strut are given by

$$
\begin{aligned}
z_{s_{fl}} &= z_s + l_f \sin\phi - t_f \sin\theta,\\
z_{s_{fr}} &= z_s + l_f \sin\phi + t_f \sin\theta,\\
z_{s_{rl}} &= z_s - l_r \sin\phi - t_r \sin\theta,\\
z_{s_{rr}} &= z_s - l_r \sin\phi + t_r \sin\theta,\\
\dot{z}_{s_{fl}} &= \dot{z}_s + \dot{\phi} l_f \cos\phi - \dot{\theta} t_f \cos\theta,\\
\dot{z}_{s_{fr}} &= \dot{z}_s + \dot{\phi} l_f \cos\phi + \dot{\theta} t_f \cos\theta,\\
\dot{z}_{s_{rl}} &= \dot{z}_s - \dot{\phi} l_r \cos\phi - \dot{\theta} t_r \cos\theta,\\
\dot{z}_{s_{rr}} &= \dot{z}_s - \dot{\phi} l_r \cos\phi + \dot{\theta} t_r \cos\theta.
\end{aligned}
\tag{11}
$$

The kinematic cross-coupling between the vehicle model and that of eARC is given by

$$
\begin{aligned}
\theta_{il} - \theta_{ir} = \sin^{-1}\left(\frac{z_{s_{if}} - z_{us_{if}}}{l_a}\right) - \\
\sin^{-1}\left(\frac{z_{s_{if}} - z_{us_{if}}}{l_a}\right).
\end{aligned}
\tag{12}
$$

IV. Field experiments

The field experiments were conducted at a proving ground with dedicated tracks for comfort and handling. Experiments were performed by driving on different sections from the comfort track and ride track. These tracks have a sufficient combined length, replicating several public road surfaces from different countries. The road conditions vary from slightly indiscrete to very severe, making it appropriate for durability verification and assessing the vehicle suspension. The vehicle is driven with a steady-state velocity, according to the speed limit for each section. The GPS signals were used for identifying the different road sections and, afterwards, to segment the recorded data. A segment of time domain measurements from one of the road sections is exemplary shown in Fig. 4.

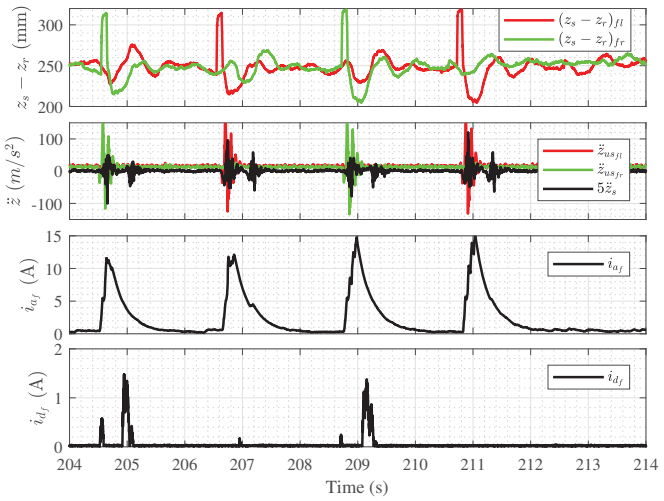

Fig. 4: Time response for a segment with phased-bumps in the end of road section.

Other relevant field-tests were conducted in a large asphalt circle with a diameter of 330 m used for vehicle handling tests under safe conditions. Constant radius cornering (CRC) tests consist in driving around a constant radius trajectory (diameter = 100 m) with a linear speed increase until reaching the handling limit of the vehicle, to see the effects of roll angle and lateral acceleration. Start-and-stop tests were also conducted for squat/dive evaluation. All field tests have been accomplished at the dedicated commercial test facilities for the ground vehicles. Further details are omitted here due to the customer specific industrial developments.

V. Identification

Identification of the derived vehicle model parameters is limited in this work to determining the lumped parameters and nonlinear characteristics from the available and experimental data. In addition, exemplary frequency response function measurements are shown for several channels to highlight the coupling effects of the complex vehicle dynamics.

A. Available lumped parameters

Lumped parameters listed in Table I have been taken over from the available technical documentations or determined from the nominal parameters of the anti-roll system and vehicle [8], [9], [13]. The mass and geometry quantities were measured during the vehicle setup.

TABLE I: Available lumped parameters

Parameter		Value	Units
m_s	Sprung mass	2495	kg
m_{us}	Unsprung mass	516.25	kg
t_f	Length from COM to corner (y_s-axis)	0.66	m
t_r	Length from COM to corner (y_s-axis)	0.70	m
l_f	Length from COM and front (x_s-axis)	1.6092	m
l_r	Length from COM and rear (x_s-axis)	1.3708	m
K_m	Torque constant	0.893	Nm/A
b_m	Viscous friction constant	10	Ns/m
J_m	Rotor moment of inertia	0.01	kg m^2
k_t	Tire elastic coefficient	250000	N/m
k_s	Spring elastic coefficient	76139.21	N/m
b_t	Tire damping coefficient	850	Ns/m
k_g	Gearbox transmission ratio	43	-
l_a	Lever length	0.300	m
I_{xx}	Moment of Inertia x-axis	250	kg m^2
I_{yy}	Moment of Inertia y-axis	2200	kg m^2

B. Nonlinear elastomer and torsion bar

The progressive nonlinear rigidity curve is mainly due to the elastomer-based decoupling unit, see [7], [8]. The elastomer decoupling unit is clearance-free flanged into the overall torsion bar assembly so that the lumped nonlinear torsion-torque characteristics in (θ_a, M_a)-coordinates can be assumed. The integrated torque sensor, used for an embedded low-level actuator torque control, provides the current torque value of the entire torsion bar. The static torsion-torque data are obtained from [8] and shown in Fig. 5 by the single data points (in green). The data points were extracted from the available curves [8] using a digitizing graph data toolbox, and an average was used as the data set for curve fitting.

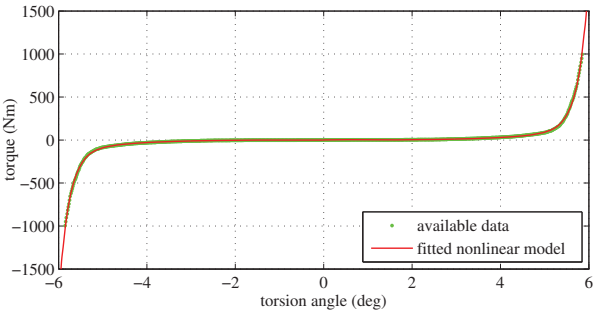

Fig. 5: Fitten nonlinear stiffness model versus available data

Based on stiffening properties of elastomers and data analysis of the torsion-torque characteristics, cf. Fig. 5, the progressive polynomial odd function

$$M_a = \sum_n \alpha_n (\beta_n \theta_a)^n, \tag{13}$$

with geometric power series of the cubic stiffness $n = 3^\gamma$ with $\gamma = \{1, 2, 3\}$, is originally proposed in this work. The abscissa and ordinate scaling parameters are β_n and α_n correspondingly. That way the smooth analytic mapping $\theta_a \mapsto f(\theta_a)$ to the restoring (or actuator) torque is provided for the entire system modeling. An accurately fitted nonlinear stiffness map (13) is shown in Fig. 5 over the used identification data.

C. Nonlinear semi-active damper

Semi-active damping systems comprise a shock absorber capable of variable damping, typically with an actuation bandwidth up to 20-30 Hz [11]. Such damping variation is achieved by an integrated electro-actuated solenoid valve. Then a system-specific force-velocity map becomes a function of the valve electronic command. Therefore, the shock absorber damping characteristics

$$F_d(\dot{z}, i_d) = f(\dot{z}, i_d, \underline{\xi}(i_d)), \tag{14}$$

depend simultaneously, in addition to a linear viscous damping, on the rod velocity $\dot{z}$ and valve current i_d. The nonlinear mapping (14) includes the set of parameters $\underline{\xi}$ to be determined from the available data set obtained experimentally in additional laboratory testing. Shock absorbers were experimentally tested in a test bench for different rod velocities and current valve openings. Based on the data analysis, the following nonlinear map

$$F_d = \xi_1 \operatorname{atan}\left(\xi_2(\dot{z} + \xi_3)\right) + \xi_4 \dot{z} + \xi_5 \tag{15}$$

is proposed, while the following polynomial coefficients p_m:

$$\begin{aligned} \xi_1 &= p_1 i_d^3 + p_2 i_d^2 + p_3 i_d + p_4, \\ \xi_2 &= p_5 i_d^4 + p_6 i_d^3 + p_7 i_d^2 + p_8 i_d + p_9, \\ \xi_3 &= p_{10} i_d + p_{11}, \\ \xi_4 &= p_{12} i_d + p_{13}, \end{aligned} \tag{16}$$

are assigned as best fitting the current-dependent parameters ξ_n, for $n = 1, \ldots, 4$. The total set of the above polynomial coefficients is fitted on the available experimental data, depicted as single points in Fig. 6. The identified smooth nonlinear damping map (15) is equally shown in Fig. 6 over the data. Considering the absolute error of the data fit $e = |F_{d_{\text{fitted}}} - F_{d_{\text{measured}}}|$, the fitted parameters were obtained with the mean value $\bar{e} = 557.04$ and the standard deviation $\sigma(e) = 419.87$.

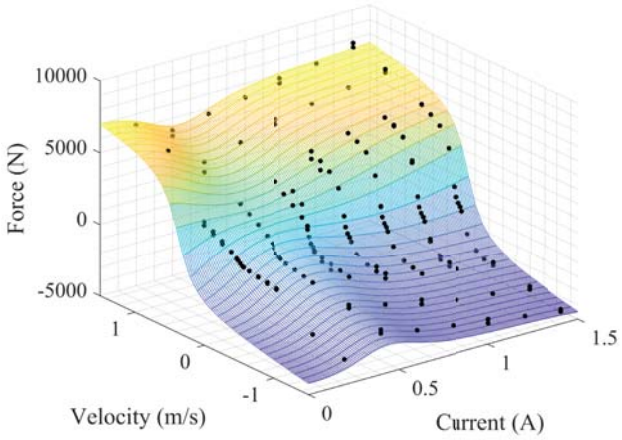

Fig. 6: Fitted nonlinear damping model versus available data

D. Linearized model

Model linearization towards a uniform MIMO (multiple-input-multiple-output) system description is made in order to allow for analysis of the frequency response characteristics and complex multi-dimensional system dynamics at large. The system described by eqs. (1)-(12) can be written in a general linear state-space representation [14]

$$\begin{aligned} \dot{x} &= Ax + Bu, \\ y &= Cx + Du, \end{aligned} \tag{17}$$

with the system matrix A, input and output coupling matrices B and C respectively, and feed-through matrix D. The derived coefficients of the above matrices are omitted here, due to the high dimensions and space limits, while the obtained numerical model (17) has been verified in simulations with the full nonlinear model given by (1)-(12). Notwithstanding, it is worth noting the components of the state vector $x \in \mathbb{R}^{18}$, input vector $u \in \mathbb{R}^{14}$ and output vector $y \in \mathbb{R}^{12}$ given by

$$\begin{aligned} x = [&\dot{z}_s, z_s, \dot{\theta}, \theta, \dot{\phi}, \phi, \dot{z}_{us_{fl}}, z_{us_{fl}}, \dot{z}_{us_{fr}}, z_{us_{fr}}, \dot{z}_{us_{rl}}, \\ &z_{us_{rl}}, \dot{z}_{us_{rr}}, z_{us_{rr}}, \dot{\theta}_{m_f}, \theta_{m_f}, \dot{\theta}_{m_r}, \theta_{m_r}]^T, \end{aligned} \tag{18}$$

$$\begin{aligned} u = [&z_{r_{fl}}, z_{r_{fr}}, z_{r_{rl}}, z_{r_{rr}}, \dot{z}_{r_{fl}}, \dot{z}_{r_{fr}}, \dot{z}_{r_{rl}}, \dot{z}_{r_{rr}}, i_{d_f}, i_{d_r}, \\ &i_{a_f}, i_{a_r}, M_{dx}, M_{dy}]^T, \end{aligned} \tag{19}$$

$$\begin{aligned} y = [&\ddot{z}_{us_{fl}}, \ddot{z}_{us_{fr}}, \ddot{z}_{us_{rl}}, \ddot{z}_{us_{rr}}, \ddot{z}_{s_{fl}}, \ddot{z}_{s_{fr}}, \ddot{z}_{s_{rl}}, \ddot{z}_{s_{rr}}, \\ &(z_s - z_r)_{fl}, (z_s - z_r)_{fr}, (z_s - z_r)_{rl}, (z_s - z_r)_{rr}]^T, \end{aligned} \tag{20}$$

correspondingly.

Small-angle approximation truncated Taylor series [15] was used for the linearization of the trigonometric functions $\sin\theta \approx \theta$, $\cos\theta \approx 1$ and $\sin^{-1}\theta \approx \theta$ for the kinematic equations given in (11) and coupling (12). Note that the relative error of this approximation is less than 1% for $\theta < 8°$.

The progressive polynomial odd function (13) is linearizated as by an equivalent stiffness coefficient

$$M_a \approx k_a \theta_a, \tag{21}$$

with k_α determined according to the actuator torque M_a range. The 3-dimensional map of the semi-active damper, see Fig. 6, was linearized as

$$F_{d_{ij}} \approx k_{\beta_v}(\dot{z}_s - \dot{z}_{us})_{ij} + k_{\beta_c} i_{d_i}, \tag{22}$$

with the corresponding coefficients k_{β_v} and k_{β_c}, which are equally subject to adjustments depending on the velocity and current operation range.

E. MIMO transfer characteristics

The linearized state-space model of the vertical dynamics, provided above in section V-D, constitutes the basis for MIMO reformulation and its further use for frequency analysis of the transfer characteristics between different input and output channels of interest. The obtained transfer function matrix $\mathbf{G}(s) = \mathbf{Y}(s)/\mathbf{U}(s)$ contains all coupling elements between the input vector $\mathbf{U}$ and output vector $\mathbf{Y}$, and $\dim(\mathbf{G}) = 12 \times 14$. By convention s is the Laplace variable, while for the measured frequency response functions the $j\omega$ argument is used, with ω to be the angular frequency and j imaginary unit of the complex numbers. Note that additional rearrangement of the input-output pairs is also possible, based on the similarity transformations, see e.g. [16], of the initial state-space model (17). This is, however, not performed in the present work since a thorough and more detailed analysis of the MIMO system is first required in order to detect and distinguish between strong (main) and weak cross-couplings.

The below frequency response functions (FRFs) are those obtained from the measured real-time data, collected during the field tests cf. sections II and IV, and estimated from the input-output channels of the full model described in section III. Note that the model input data are taken from the same measured experimental data set. In the following we demonstrate the frequency characteristics of one exemplary taken output of interest, $\ddot{z}_{s_{rr}}$, and that for three different inputs i_{d_r}, i_{a_r}, and M_{dx}. Here, a drive experiment with constant cornering and increasing lateral acceleration is taken into consideration. Note that at those drive conditions, the momentum M_{dx} provides a persistent excitation while both control values i_{d_r} and i_{a_r} on the rear axle are equally subject to an intensive dynamic behavior owing to the anti-roll support in operation. The transfer function estimate is computed, in a standard way, as the ratio of the output Fourier transform to the input Fourier transform of the time series. A slightly smoothing effect, for the sake of a better visualization, is obtained by additionally applying a high-dimension Hamming window to the Fourier transformed data.

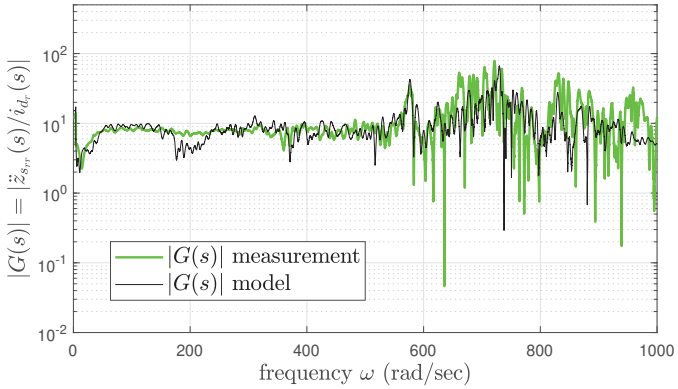

(a)

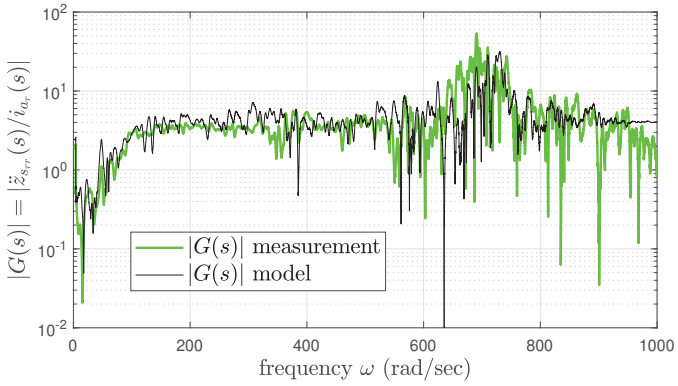

(b)

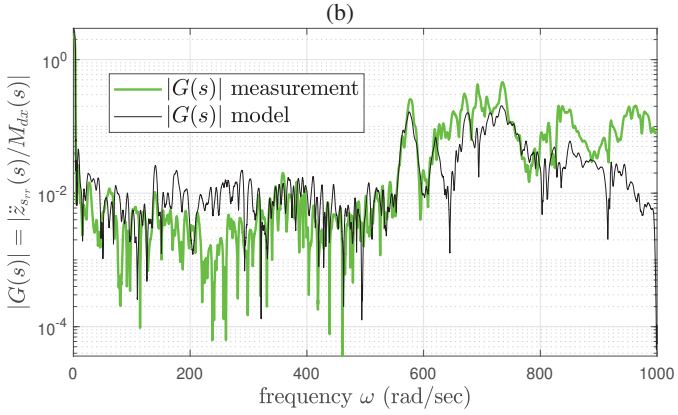

(c)

Fig. 7: Measured frequency response characteristics, $\ddot{z}_{s_{rr}}/i_{d_r}$ in (a), $\ddot{z}_{s_{rr}}/i_{a_r}$ in (b), and $\ddot{z}_{s_{rr}}/M_{dx}$ in (c).

All three frequency responses, for the measured data of drive experiments and for the full model of vertical dynamics given in eqs. (1)-(12), are shown in Fig. 7. Since these transfer characteristics have all the input and output quantities equivalent to the generalized forces, no free differentiator or integrator behavior can be consequently expected and observed. The most pronounced resonance peak is visible in the $\ddot{z}_{s_{rr}}/i_{a_r}$ transfer characteristics, and appears reasonable due to the stiffness of torsion bar. Several distortions in the amplitude response point on the coupling effects of multi-body dynamics and relatively high level of both the process

and measurement noise. At the same time, a relatively high overlapping of both, measured and model estimated, FRFs can be seen over the whole frequency range of about 1000 Hz.

Another set of drive experiments was also evaluated on dedicated sections of the straight road, aiming to replicate driving in standard public roads with typical driving conditions (e.g. vehicle velocity). Here not so much influence from high lateral momentum M_{dx} is present, but rather the contribution of the semi-active damper and active torsion bar which operate to filter out the road disturbances. For another selected output of interest $\ddot{z}_{s_{fl}}$, the estimated frequency response characteristics, from the measured experiments and simulated model eqs. (1)-(12), are exemplary shown in Fig. 8 for the inputs i_{d_f} and i_{a_f}. Certain discrepancies in the resonance peaks range are observed, which can be reasonably attributed to: the conditioned information and measurements of the road excitation, cross-coupling effects, and measurement noise and uncertainties of the fitted model parameters.

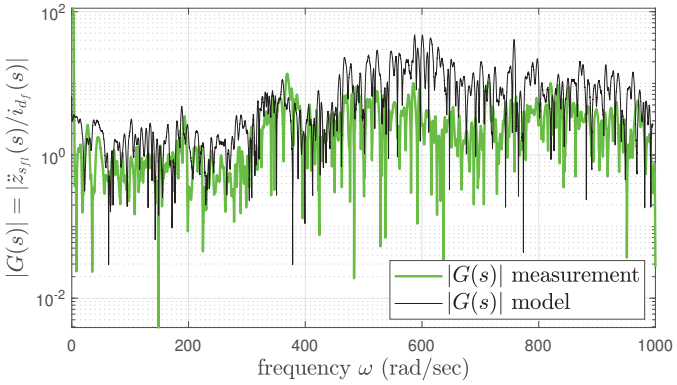

(a)

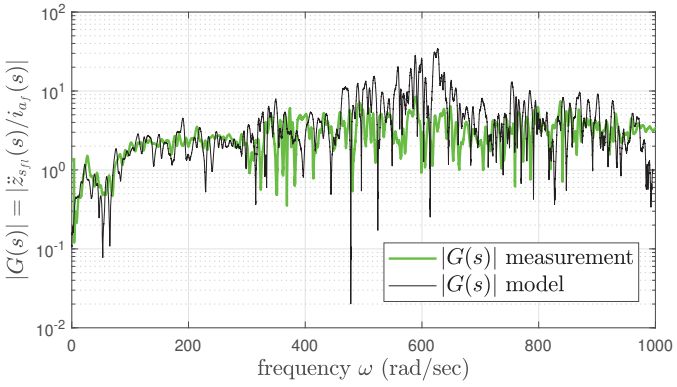

(b)

Fig. 8: Measured frequency response characteristics, $\ddot{z}_{s_{fl}}/i_{d_f}$ in (a) and $\ddot{z}_{s_{fl}}/i_{a_f}$ in (b).

VI. Conclusions

In this paper, we derived the full vertical vehicle model with the integrated anti-roll bar and semi-active suspension. The obtained model is nonlinear and can be seen as full-scale since capturing all main sources and internal terms of the coupled multi-body system dynamics. Also the corresponding linearized MIMO model is obtained which is, however, subject to further studies and refinements concerning the cross-coupling and linearization by-effects. Two analytic forms of nonlinear mapping used for the key components of the active anti-roll suspension system have been proposed and accurately fitted with experimental data. The series of accomplished field-experiments of a full-scale drive has been described along with the vehicle setup, instrumentation, and measurements. The demonstrated comparison between the measured and model-estimated frequency response characteristics, for different multiple input-output channels, disclose the sufficient generality and fidelity of the whole model, that over a relatively large frequency range.

Acknowledgment

This work has received funding from the European Union Horizon 2020 research and innovation programme H2020-MSCA-RISE-2016 under the grant agreement No 734832.

References

[1] D. Karnopp, "Active damping in road vehicle suspension systems," *Vehicle System Dynamics*, vol. 12, no. 6, pp. 291–311, 1983.

[2] P. S. Els, N. J. Theron, P. E. Uys, and M. J. Thoresson, "The ride comfort vs. handling compromise for off-road vehicles," *Journal of Terramechanics*, vol. 44, no. 4, pp. 303–317, 2007.

[3] R. Isermann, "Mechatronic systems – innovative products with embedded control," *Control Engineering Practice*, vol. 16, no. 1, pp. 14–29, 2008.

[4] H. E. Tseng and D. Hrovat, "State of the art survey: active and semi-active suspension control," *Vehicle system dynamics*, vol. 53, no. 7, pp. 1034–1062, 2015.

[5] M. Strassberger and J. Guldner, "BMW's dynamic drive: an active stabilizer bar system," *IEEE Control Systems Magazine*, vol. 24, no. 4, pp. 28–29, 2004.

[6] V. T. Vu, O. Sename, L. Dugard, and P. Gáspár, "Enhancing roll stability of heavy vehicle by lqr active anti-roll bar control using electronic servo-valve hydraulic actuators," *Vehicle system dynamics*, vol. 55, no. 9, pp. 1405–1429, 2017.

[7] U. Grau and R. Mayer, "Geared motor for an active roll stabilizer," Patent, 2009, US8690174B2 Patent.

[8] M. Stiegler, "Electromechanical active roll control – developing the future," in *7th International Munich Chassis Symposium 2016*. Springer, 2017, pp. 107–123.

[9] H. Huang, M. Hartmann, H. F. Awad, and D. Knetsch, "Virtual functional testing of a mechatronic active roll control," SAE Technical Paper, Tech. Rep., 2018.

[10] R. Tavares, J. Molina, M. Al Sakka, M. Dhaens, and M. Ruderman, "Modeling of an active torsion bar automotive suspension for ride comfort and energy analysis in standard road profiles," in *8th Symposium on Mechatronic Systems and 11th Symposium on Nonlinear Control Systems*. IFAC, 2019, pp. 181–186.

[11] S. M. Savaresi, C. Poussot-Vassal, C. Spelta, O. Sename, and L. Dugard, *Semi-active suspension control design for vehicles*. Elsevier, 2010.

[12] T. Shim and C. Ghike, "Understanding the limitations of different vehicle models for roll dynamics studies," *Vehicle system dynamics*, vol. 45, no. 3, pp. 191–216, 2007.

[13] S. Sagewka, T. Fiebig, C. Schmid, and D. Wostal, "Mechatronic roll control for the 48-v electrical system," *ATZ worldwide*, vol. 119, no. 3, pp. 58–63, 2017.

[14] K. Ogata, *Modern Control Engineering*, ser. Instrumentation and controls series. Prentice Hall, 2010.

[15] T. M. Apostol, *Calculus, Volume I, One-variable Calculus, with an Introduction to Linear Algebra*. John Wiley & Sons, 2007, vol. 1.

[16] J. M. Maciejowski, *Multivariable feedback design*, ser. Electronic Systems Engineering Series. Addison-Wesley, 1989.